



Cite this: *RSC Adv.*, 2019, 9, 899

New aspects of improving the performance of WO₃ thin films for photoelectrochemical water splitting by tuning the ultrathin depletion region†

Jiajie Cen,^a Qiyuan Wu,^a Danhua Yan,^{ab} Wenrui Zhang,^b Yue Zhao,^c Xiao Tong,^b Mingzhao Liu^{*b} and Alexander Orlov^{*a}

In this work, we explored a facile, scalable and effective method for substantially enhancing photocurrent and incident-photon-to-current efficiency of WO₃ thin-film photoanodes by a mild reduction treatment under low oxygen pressure. Experimental data from photoelectrochemical and electrochemical impedance spectroscopies have shown that such treatment can increase the charge carrier density on WO₃ photoanode surfaces resulting in improvements in hole collection efficiency and reduction in charge recombination. Despite a much thinner layer of WO₃ (about 500 nm) compared to those in other published studies, the electrodes exhibited an ultra-high photocurrent density of 1.81 mA cm⁻² at 1.23 V vs. RHE. This current density is one of the highest ones among WO₃-based photoanodes described in literature. The proposed surface modulation approach offers an effective and scalable method to prepare high-performance thin film photoanodes for photoelectrochemical water splitting.

Received 25th October 2018
 Accepted 17th December 2018

DOI: 10.1039/c8ra08875f

rsc.li/rsc-advances

1. Introduction

Water splitting in photoelectrochemical (PEC) cells is potentially the most promising method for converting solar energy into chemical energy. Tungsten trioxide (WO₃), which is an n-type semiconductor, is one of the most promising candidate materials for PEC water oxidation.¹ This semiconductor has an indirect band gap of 2.5–2.8 eV while being among only a few visible-light-responsive photocatalysts that exhibit outstanding stability in acidic electrolytes (pH ≤ 4). In contrast, other visible-light activated photoanode materials, such as BiVO₄ and α-Fe₂O₃, are less stable under the same acidic conditions. This is important as photoanodes with significant stability in acidic environments (e.g. WO₃) could be utilized in acidic water electrolyzers based on polymer electrolyte membranes, which overcomes many of the disadvantages of the conventional alkaline electrolyzers.² The disadvantages of WO₃ based anodes stem from their indirect band gap. As a result, WO₃ exhibits a weak light absorption in visible range (α = 10⁴ to 10⁵ cm⁻¹), which is about one order of magnitude lower than that of other visible light photocatalysts, such as Fe₂O₃ and BiVO₄. This disadvantage can be potentially offset by having a relatively long

(~500 nm) hole diffusion length in the WO₃ materials, thereby conceivably offering a more efficient carrier delivery from bulk to depletion region. The overall result of a combination of unfavorable weak light adsorption and favorable diffusion length is that most of the incident photons interacting with WO₃ photoanodes are absorbed beyond the depletion region, resulting in an insufficient charge carrier separation despite the carrier's high mobility.

In the past WO₃ photoanodes were usually prepared as thick films (typically a few micrometers in thickness) to overcome the weak visible light absorption.^{3–13} Other attempts to improve absorption included tuning the illuminated surface area by introducing surface microstructures,^{6,14–17} which might not be a practical and scalable way forward. In addition to tuning light absorption on photoanode, another strategy to improve the photocurrent is to overcome the kinetic limitation in O₂ evolution by introducing modification on the photoanode surface with appropriate co-catalysts. Among a few examples of oxygen evolution catalysts deposited on WO₃, Bi₂S₃, Sb₂S₃, CoO_x, FeOOH, and IrO₂ are the most promising ones, with only IrO₂ offering good stability in acidic electrolyte.^{18–24} While exhibiting an improved oxygen evolution performance, these catalysts also reduce the photon flux reaching WO₃ due to their non-transparent nature.^{25,26} Therefore, the potential improvements for oxygen evolution by surface-decorated co-catalyst is offset by reduced light absorption. In addition to modifying surfaces, adding catalysts to electrolytes was also explored. It was found that both phosphotungstate and phosphomolybdate improved the WO₃ photoanode performance.²⁷ However, despite some success in using the above mentioned strategies,

^aDepartment of Materials and Science Engineering, Stony Brook University, Stony Brook, New York, 11794, USA. E-mail: alexander.orlov@stonybrook.edu

^bCenter for Functional Nanomaterials, Brookhaven National Laboratory, Upton, New York, 11973, USA. E-mail: mzliu@bnl.gov

^cDepartment of Chemistry, Stony Brook University, Stony Brook, New York, 11794, USA

† Electronic supplementary information (ESI) available. See DOI: 10.1039/c8ra08875f



it is still a challenge to develop highly efficient visible light absorbing photoanodes with very transparent oxygen evolution catalysts that can also offer thermodynamic stability in acidic electrolytes.¹⁸

In order to move this field further, it is important to critically evaluate the mechanistic aspects of the current electrode design strategies. In our work, we address a specific challenge of improving the PEC activity of unmodified WO₃ electrode without creating a thick film electrode geometry, which causes photon adsorption beyond the carrier diffusion region. Introduction of oxygen vacancies to the surface of semiconductors can be one promising strategy to improve WO₃ photocatalytic efficiency while keeping relatively thin thickness.²⁸ Oxygen vacancies typically act as donor defects for n-type oxides, where they exert a significant influence on space charge region (SCR) and charge recombination.^{11–13,29} In addition, dual oxygen and tungsten vacancies have proven to significantly enhance the hole transfer efficiency at semiconductor electrolyte interface (SEI).⁴ Therefore, modulating the functions of vacancies at the surface of semiconductors using a finely controlled method can be a potentially promising way forward to design high performance thin film PEC electrodes. The novel aspects of this study are in developing sophisticated performance tuning of WO₃ electrodes by simultaneous fine adjustment of both oxygen vacancies and thickness of the oxide layer, while maintaining a good crystallinity of the sample. Here we introduce a simple surface reduction method that can significantly enhance the performance of bare WO₃ thin film photoanodes, which are only 500 nm thick. These photoanodes showed a performance similar to that of other literature described WO₃ photoanodes with few micrometers in thickness. Our results demonstrate that a sophisticated control of the electrode surfaces reduction is necessary to further optimize water oxidation activity of WO₃ photoanodes.

2. Results and discussion

Fabrication of the water splitting photoanodes was accomplished by depositing WO₃ thin films on ITO glass substrates using pulsed laser deposition (PLD). The thicknesses of the WO₃ thin films were controlled by the total number of laser pulses. The conditions of thin film deposition were optimized based on PEC measurements on as-deposited WO₃ photoanodes (Fig. S2, ESI†). Following the PLD deposition, the film was annealed under decreased partial oxygen pressure (*p*O₂) of 95 mTorr to achieve surface reduction (Fig. 2a). This approach was consistent with published strategy of adjusting WO_{3–x} composition by tuning (*p*O₂) during annealing. Samples reduced for 0, 200, 400, and 600 seconds under 95 mTorr of *p*O₂ were labelled as R0 (pristine), R1, R2, and R3 respectively. The as-deposited pristine WO₃ film exhibited an intrinsic optical absorption up to 450 nm (Fig. 1c), which according to the Tauc plot indicates an indirect band edge at 2.7 eV. The X-ray diffraction (XRD) patterns collected from the thin films were indexed as monoclinic WO₃ (PCPDF# 72-1465), and the strongest diffraction signal consistently arose from the (002) plane, indicating it as the preferred domain orientation (Fig. S4b,

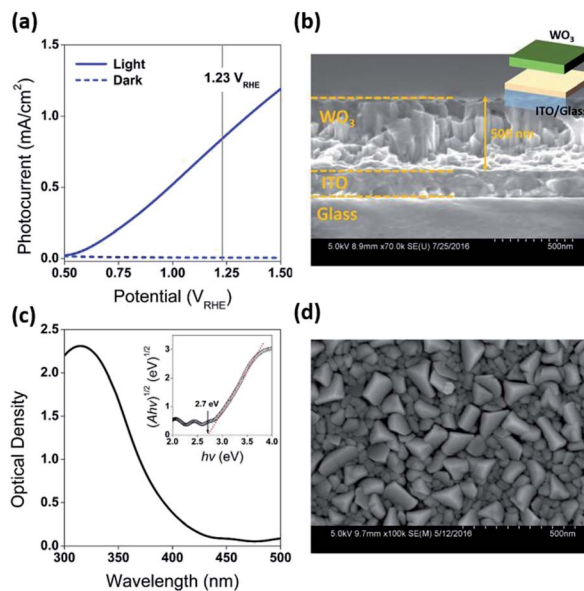


Fig. 1 (a) Current density vs. potential under front-side AM 1.5 illumination for the as-prepared WO₃ photoanodes (R0). The vertical line indicates the thermodynamic potential for oxygen evolution (1.23 V_{RHE}). (b) Cross-sectional SEM image of WO₃ thin film sample prepared by 40k laser pulses. (c) UV-vis spectrum of as-prepared WO₃ photoanodes (R0) with Tauc plot inserted. (d) SEM image of as-prepared WO₃ photoanodes (R0).

ESI†). The Raman spectra (Fig. S4c, ESI†) show the most intense bands at 805 cm⁻¹ and 715 cm⁻¹ were assigned to O–W–O stretching vibrations, while the bands at 274 cm⁻¹ and 332 cm⁻¹ were assigned to O–W–O bending vibrations.^{30–33} The scanning electron microscopy (SEM) image (Fig. 1d) showed high uniformity of the WO₃ thin film morphology. The cross-sectional SEM image of WO₃ thin film sample prepared by 40k laser pulses (Fig. 1b), which included ITO bottom electrode,

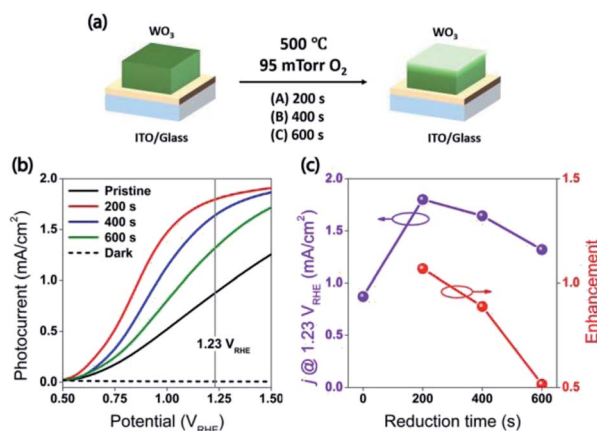


Fig. 2 (a) The illustration of mild reduction treatment. (b) Current density vs. potential under front-side AM 1.5 illumination for the WO₃ photoanodes, R0, R1, R2, and R3. The vertical line indicates the thermodynamic potential for oxygen evolution (1.23 V_{RHE}). (c) The photocurrent of the WO₃ photoanodes (R0, R1, R2, and R3) at 1.23 V_{RHE}, and the relative enhancements for the reduced WO₃ photoanodes (R1, R2, and R3). The characterization of the photoanodes were conducted in 0.5 M H₂SO₄ electrolyte.



indicated that its thickness was about 500 nm. After the reduction treatment, no significant differences in UV-vis, XRD and Raman of the reduced samples were observed (Fig. S4, ESI†). The lattice spacing calculated from the high-resolution TEM (HRTEM) images (Fig. 4c and f) was 3.90 Å, corresponding to the distance between the (002) planes of a monoclinic WO_3 phase.

The water splitting properties of the WO_3 thin film photoanodes were studied by photoelectrochemical methods. According to the current density–potential (J - E) curves, which were measured in a 0.5 M H_2SO_4 solution ($\text{pH} = 0.3$) under front-side (electrolyte–electrode side, EE) AM 1.5G illumination (Fig. 2b and c), all the WO_3 photoelectrodes produced anodic photocurrents that were consistent with the n-type doping. The onset potentials of all photoanodes were approximately 0.50 V_{RHE} . The sample treatment in reduced atmosphere significantly improved photocurrents (samples R1, R2 and R3). The sample R1, which was annealed for 200 s, exhibited the largest photocurrent (1.80 mA cm^{-2} at 1.23 V_{RHE}), which was 2 times higher than that of the pristine sample. Increasing annealing time to 400 and 600 s, resulted in photocurrent decrease for samples R2 and R3. Additional insights into the observed trends were provided by the incident-photon-to-current efficiency (IPCE) measurements. Fig. 3 shows a dependence of the IPCE at 1.23 V_{RHE} on the excitation wavelength. A comparison between pristine (R0) and mildly reduced (R2) samples shows that R1

exhibited improved IPCE across the entire spectral range (300–480 nm). Fig. 3c shows the ratio of IPCE values for sample R1 : R0 as a function of the excitation wavelength and applied potential. It showed more than 4-fold enhancement in IPCE at 425 nm measured at lower applied potential. The maximum enhancement was up to 12 times at about 0.9 V_{RHE} . In contrast to significant differences in the 300–340 nm spectral region between the sample reduced for the shortest period of time (R1) and the ones reduced for a longer time (R2 and R3), all the other samples showed a similar IPCE in the spectral range of 340–480 nm. Therefore, one can conclude that lower photocurrents for R2 and R3 samples as compared to that for R1 sample (Fig. 2b) can explain the sub-optimal performance of R2 and R3 electrodes (Fig. 3d) in the 300–340 nm spectral range. The results also suggest that there is an optimal duration of electrodes treatment in the reducing atmosphere that maximizes the IPCE in the visible light region.

In order to understand the effect of electrodes' treatment on their structure, morphology and surface composition, a further characterization of the samples was performed by X-ray diffraction, X-ray Photoelectron Spectroscopy (XPS), Atomic Force Microscope (AFM) and Electrochemical Impedance Spectroscopy (EIS). No new X-ray diffraction peaks or significant peak shift in the existing peaks were observed for the reduced WO_3 samples (Fig. S4a–c, ESI†), suggesting that the reduction treatment had a minimal effect on WO_3 lattice structure. The surfaces of the pristine and reduced WO_3 samples were further investigated by atomic force microscopy. The average surface roughness (R_a) for R0, R1, R2 and R3 samples was 4.5, 4.2, 5.1, and 5.4 nm, respectively. Despite the fact that the surfaces of R0, R1, and R2 samples appeared to have very similar granular structures, these structures were not present in the R3 sample reduced for the longest time (Fig. 5a–d). These results suggest that the reduction treatment has some subtle effects on WO_3 morphology, although defining the trends in morphological changes might require further investigation. The effect of sample reduction on the WO_3 surface composition was further studied by the XPS in conjunction with EIS measurements. Fig. 6a–d shows high-resolution W 4f spectra of the WO_3 photoanodes (R0, R1, R2, and R3). It can be clearly seen that the WO_3 undergo significant evolution upon the reduction

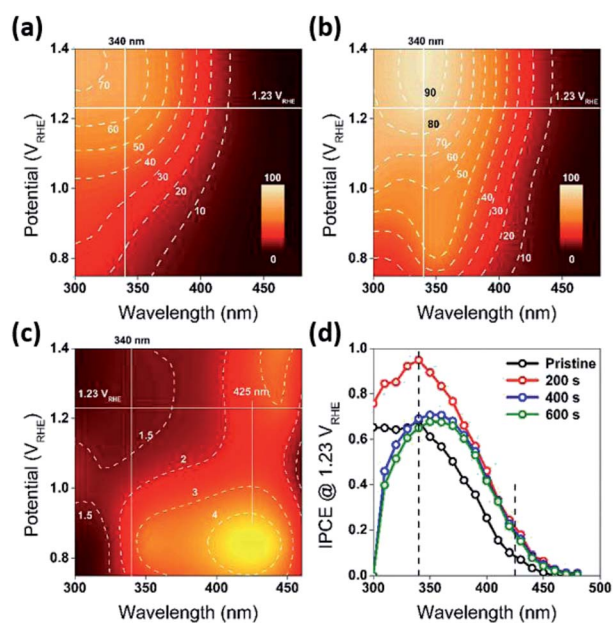


Fig. 3 (a and b) Front-side (EE) IPCE as a function of excitation wavelength potential, for the R0 (Pristine) and R1 (reduced for 200 s) WO_3 photoanodes. Both the panels share the same color scale. The dashed lines are contours for corresponding IPCE values in percentage. (c) The ratio of IPCE values for sample R1/R0. The dashed lines are contours for corresponding enhancement of IPCE values. The horizontal white lines indicate the thermodynamic potential for oxygen evolution (1.23 V_{RHE}). (d) Front-side (EE) IPCE measurements for the WO_3 photoanodes (R0, R1, R2, and R3), carried out at 1.23 V_{RHE} . The characterization of the photoanodes were conducted in 0.5 M H_2SO_4 electrolyte.

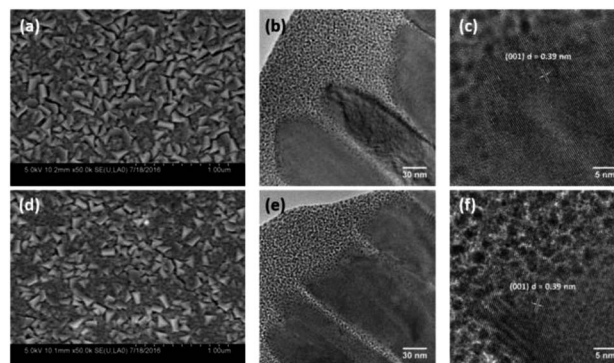


Fig. 4 SEM and cross-sectional HRTEM (a–c), of pristine WO_3 (R0) and (d–f), reduced WO_3 (R3) photoanodes.



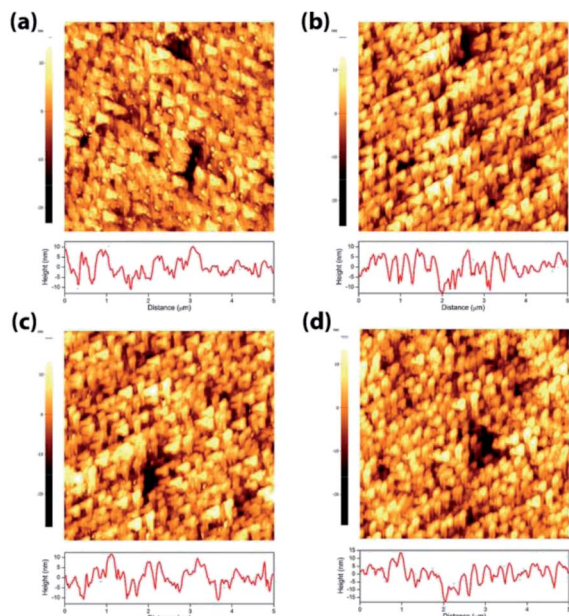


Fig. 5 AFM for WO₃ photoanodes (R0, R1, R2, and R3).

treatment. The W 4f doublet at 37.7 and 35.5 eV, can be assigned to W⁶⁺ species, while 36.5 and 34.3 eV doublet can be assigned to W⁵⁺ species. A comparison between W 4f peaks

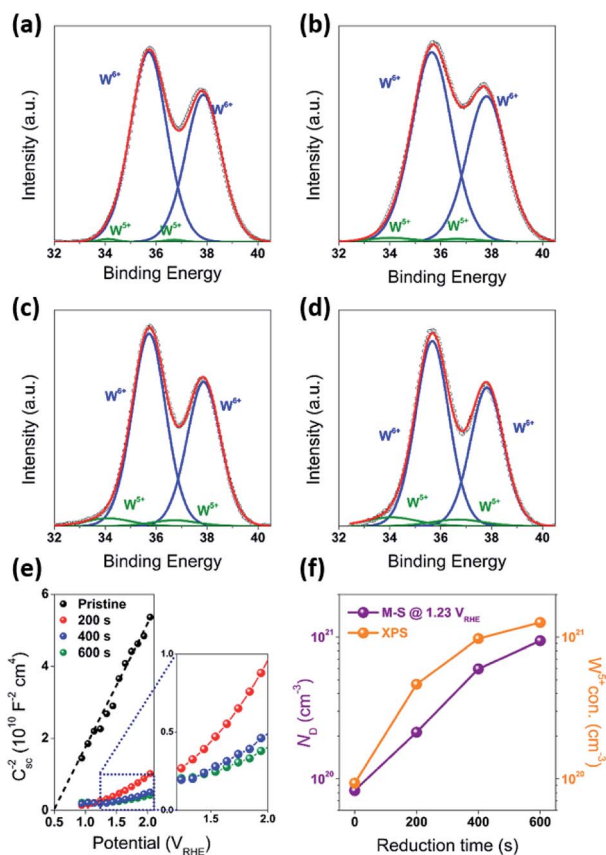


Fig. 6 (a–d) W 4f XPS for WO₃ photoanodes (R0, R1, R2, and R3). (e) Mott–Schottky plots, for pristine and WO₃ photoanodes (R0, R1, R2, and R3). (f) N_D and W⁵⁺ concentration as a function of reduction time.

for samples reduced for different times (R1–R3) indicated an increased full width at half maximum (FWHM) of the peaks as compared to that for the pristine sample (R0). Such increase can be attributed to increased contribution of W⁵⁺ species to the overall spectra with increased reduction time (Fig. 6f). More specifically, the W⁵⁺ concentration was determined based on the ratio of W⁶⁺ and W⁵⁺ peak areas. The pristine sample (R0) had W⁵⁺ atomic concentration of 0.5%, (9.2×10^{19} cm⁻³, W⁵⁺ concentration in volume), while the most reduced sample (R3) had an increased W⁵⁺ atomic concentration of species of 6.8%, (1.26×10^{21} cm⁻³ W⁵⁺ concentration in volume). It is important to note that the presence of W⁵⁺ species is indicative of oxygen vacancies formation, which act as shallow donors for n-type WO₃.³⁴ In order to understand the effect of oxygen vacancies on PEC performance, the donor densities were determined by EIS, which measured the differential capacitance C_{sc} of the depletion region at various electrode potentials E . For a flat, uniformly doped semiconductor electrode, a linear relation between $1/C_{sc}^2$ and E is defined by the Mott–Schottky equation:^{24,35–37}

$$\frac{1}{C_{sc}^2} = \frac{2}{e\epsilon\epsilon_0 N_D} \left(E - E_{FB} - \frac{k_B T}{e} \right) \quad (1)$$

In our case, this equation was used to determine the donor density N_D based on such variables as elementary charge e , the dielectric constant ϵ , the vacuum permittivity ϵ_0 , the flat band potential E_{FB} and the thermal energy $k_B T$. In our calculations the value of $\epsilon = 35$ for the WO₃ electrodes was based on the literature data.¹⁵ The N_D value for the pristine sample (R0) was 8.3×10^{19} cm⁻³ with $E_{FB} = 0.5$ V_{RHE}, while N_D values increased monotonically with an increased exposure time to reducing atmosphere. More specifically, the N_D values for the reduced samples R1, R2, and R3 were 2.1×10^{20} , 6.0×10^{20} and 9.4×10^{20} cm⁻³ respectively. It is useful to note that the donor densities determined by the EIS method were within one order of magnitude of W⁵⁺ surface densities determined by XPS, confirming a successful introduction of tunable concentration of oxygen vacancies into the WO₃ surfaces by a very simple treatment.

To clarify the mechanism of the PEC enhancement by the mild reduction treatment, several factors have to be considered. Previously published modification of WO₃ by various treatment methods introduced H_xWO₃ and/or WO_{3-x} (W⁵⁺ and oxygen vacancies) species into WO₃ photoanodes, which resulted in the enhancement of PEC water oxidation.^{4,28,38,39} Although the studies mentioned above focused on photoanodes having different film thickness and surface pre-treatment conditions from those used in this work, it is still instructive to analyze these published results. More specifically the literature suggests that the WO₃ photoanodes containing W⁵⁺ species are highly resistive to re-oxidation and peroxy-species induced dissolution,²⁸ while exhibiting enhanced hole transfer efficiency.^{4,38,39} Our calculations based on Butler–Volmer model⁴⁰ also showed that the mild reduction treatment on WO₃ can also enhance the absolute magnitude of the electric field (E_0) at the interface



between semiconductor and electrolyte (Fig. S6a, ESI[†]), resulting in suppressing of electron collection efficiency (Fig. S6b, ESI[†]).⁴⁰

In addition to the above mentioned electronic effects, it is also important to consider such spatial factors as depletion width, effective minority carriers diffusion and the thickness of the higher dopant density region. These spatial factors can all be affected by the surface treatment. For example, reduction of the samples resulted in an increase in dopant concentration and decrease in a depletion width. At 1.23 V_{RHE} , the calculated depletion width (d_{sc}) of pristine WO_3 (R0) electrode was about 7 nm, while the d_{sc} for the reduced WO_3 (R1, R2, and R3) electrodes was about 2 nm (Fig. S6c, ESI[†]). In the classic Gartner model, photocurrent may only be produced when photo-generated charge carriers are created within both the depletion width and effective minority carrier diffusion length (L_p). Given that the literature reported hole diffusion length for WO_3 is $L_p = 0.5 \mu\text{m}$.^{7,40,41} while the measured sample thickness is also 0.5 μm , it is conceivable that all photogenerated holes were efficiently utilized as charged carriers that could diffuse into SCR. However, such efficient utilization of holes can't explain the difference in photocurrent and IPCE between R1, R2, and R3 electrodes, where the presence of the doped region did not improve the quantum efficiency or R2 and R3 samples across the entire spectrum. As evident from Fig. 3d, a thicker reduction region for R2 and R3 electrodes resulting from longer reduction times caused a precipitous decrease in IPCE within 300 nm to 340 nm wavelength window (Fig. 3d). To rationalize this dependence, it is important to emphasize that a mismatch between depletion and doped region widths is critical to explain such behavior. Considering that in our case the doped region is larger than the depletion region, the recombination sites for doped region of R2 and R3 electrodes most likely suppressed and quenched the photogenerated charge carriers excited by the shorter wavelength light in the 300–340 nm spectral region. However, for the mildly reduced WO_3 photoanode (R1) it is conceivable that the reduction region has a better match to a depletion region. As result, the R1 electrode exhibited dramatic across 300–480 nm wavelength IPCE enhancement as compared to that for the pristine sample (Fig. 7c and d).

To get further understanding of the charge carriers' dynamic of at the SEI, photoelectrochemical impedance spectroscopy (PEIS) measurements were conducted at the PEC experimental conditions under illumination. These measurements allowed to model several aspects of an electrode behavior. As compared to the often used EIS equivalent model for dark condition (Fig. S5, ESI[†]), the equivalent circuit model utilized this our work (Fig. S7, ESI[†]) contains additional variables that reflect behaviors of the traps in photoanodes. These variables include a chemical capacitance (C_{ss}) representing the chemical capacitance of the traps, a trapping resistance (R_{trap}) representing the trapping/detrapping resistance of electrons that go from the conduction band to the surface traps, and a charge-transfer resistance (R_{ct}) representing the resistance of hole transfer.^{42,43} The dependence of these variables (C_{ss} , R_{trap} , and R_{ct}) on the applied potential measured for our samples is shown in the ESI (Fig. S7, ESI[†]). In order to get better insights from this

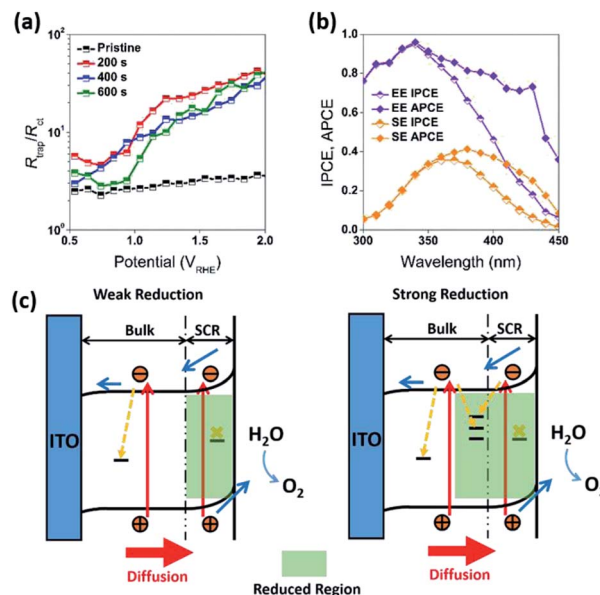


Fig. 7 (a) $R_{\text{trap}}/R_{\text{ct}}$ for R0, R1, R2, and R3 photoanodes under front-side (EE) illumination. (b) Back-side (semiconductor–electrolyte side, SE) and front-side (EE) IPCE and APCE measurements for the optimized WO_3 photoanodes (R1), carried out at 1.23 V_{RHE} . The characterization of the photoanodes were conducted in 0.5 M H_2SO_4 electrolyte. (c) Schematic band bending diagram and charge transfer processes in WO_3 photoanodes after weak and strong reduction treatments.

dependence, it is informative to relate the hole collection efficiency to the ratio $R_{\text{trap}}/R_{\text{ct}}$,⁴⁴ as following:

$$\frac{R_{\text{trap}}}{R_{\text{ct}}} \propto \frac{k_s}{\varepsilon_n} \quad (2)$$

where k_s is the rate of charge transfer and ε_n is the rate of recombination. This ratio can also be used to reflect the kinetics of water oxidation at photoanode surface.^{24,42,44,45} As shown in Fig. 7a, the ratios of $R_{\text{trap}}/R_{\text{ct}}$ for pristine and reduced WO_3 photoanodes generally increased as the applied potential increased, while the minimum values of this ratio were observed at the onset potential (0.5 V_{RHE}) (Fig. 6a). As the applied potential increased, the ratios of $R_{\text{trap}}/R_{\text{ct}}$ for the reduced WO_3 photoanodes (R1, R2, and R3) became more than one order of magnitude higher than that of the pristine WO_3 photoanode (R0) (Fig. 7a). Among the three reduced samples (R1, R2, and R3), the R1 sample exhibited notably higher $R_{\text{trap}}/R_{\text{ct}}$ ratios than those for R2 and R3 samples. Such enhancement implies that a reduced WO_3 surface tends to exhibit a higher rate of charge transfer. Moreover, the additional experiments on the R1 sample also indicated its high stability (Fig. S10a–c, ESI[†]). The observed trends in kinetics and stability are also consistent with previous studies demonstrating that a sub-stoichiometric WO_{3-x} region at the WO_3 electrode surface can dramatically enhance both photocurrent and photostability.^{4,29,46} This observation also suggests that by controlling the mild reduction duration, the charge transfer rate can be increased, which can positively contribute to the photocurrent and IPCE improvement.



3. Conclusion

In summary, WO₃ thin film photoanodes were prepared by pulsed laser deposition under optimized conditions. The mild reduction treatment on WO₃ photoanodes was controlled by post annealing in low oxygen partial pressure for different durations. The surface reduced of the samples was characterized by Mott–Schottky, XPS, PEC and IPCE measurements. The results work outlined the optimum conditions for the surface reduction treatment, as elevated level of defects beyond the space charge region resulted in loss of IPCE in UV region. The mildly reduced R01 sample exhibited largely improved PEC photocurrent density and IPCE across the entire 300–480 nm spectral window. This work provides a simple and well-defined roadmap for the preparation of high performance WO₃ photoanodes by mild surface modulation. This approach might be also promising for other semiconductors with small dielectric constants, which can potentially include α -Fe₂O₃ and TiO₂ based electrodes.

4. Experimental section

4.1 Thin film fabrication

WO₃ thin films were grown by pulsed laser deposition (PLD/MBE-2300, PVD Products) on indium tin oxide (ITO) glass substrates (Thin Film Devices, 20 Ω sq⁻¹). More specifically, a ceramic WO₃ target was prepared by cold-pressing WO₃ powder into a cylindrical pellet, which was finally sintered at 1100 °C for 12 hours. The WO₃ target was ablated by KrF excimer laser pulses ($\lambda = 248$ nm) at a fixed repetition rate of 5 Hz, with a laser fluence of 1.5 J per cm² per pulse. The substrate was placed 60 mm away from the target and heated to 500 °C by a non-contact radiative heating system under a controlled oxygen pressure (10–300 mTorr). The deposition rate for WO₃ was about 0.15 Å per pulse. After the deposition, the substrate was cooled down at a constant rate of 10 °C min⁻¹ to a room temperature. The surface of the samples was reduced by post annealing at 500 °C under 95 mTorr oxygen pressure for 200–600 seconds. Samples reduced for 0, 200, 400, and 600 seconds were labelled as R0, R1, R2, and R3 respectively.

4.2 Characterization

The X-ray diffraction patterns were recorded by an Ultima III diffractometer with parallel beam optics using Cu-K α radiation ($\lambda = 1.54184$ Å). Optical characterization was performed in a Lambda 950 UV-vis-NIR spectrometer (PerkinElmer) equipped with a 150 mm integrating sphere. Scanning electron microscopy images were obtained using a HITACHI 4800 SEM at an accelerating voltage of 10 kV. The cross sections of the samples were prepared by focused ion beam *in situ* liftout using an FEI Helios dual beam SEM-FIB system. The X-ray photoelectron spectroscopy was performed in an ultra-high vacuum (UHV) chamber equipped with a hemispherical electron energy analyzer (Thermo Fisher Scientific, Alpha 110) and an Al/Mg twin anode X-ray source (Thermo Fisher Scientific, T352/NT).

4.3 Photoelectrochemical measurements

PEC measurements were performed in a custom-built, three-electrode cell with a quartz viewing window. The cell included a working photoanode, an Hg/Hg₂SO₄/saturated K₂SO₄ reference electrode (0.640 V_{NHE}, WPI Inc.), and a platinum wire counter electrode. A 1.0 cm² area of the working electrode was exposed to the electrolyte and illuminated from the front-side through the quartz window or the back-side through the ITO glass. The electrolyte was an aqueous solution of 0.5 M H₂SO₄ (pH \sim 0.3). The linear sweep voltammetry (LSV) was performed with a sweep rate of 50 mV s⁻¹ under dark or under simulated AM 1.5G illumination, using a Newport-Oriel 150 W Xenon arc lamp fitted with an AM 1.5G filter. The incident illumination power of 100 mW cm⁻² was measured by a calibrated Si detector (Newport). The potentials referenced to the Hg/Hg₂SO₄ reference electrode were converted to potentials referenced to the reversible hydrogen electrode (RHE) using the Nernst equation,

$$E_{\text{RHE}} = E_{\text{Hg/Hg}_2\text{SO}_4} + 0.0591 V \times \text{pH} + 0.682 V \quad (3)$$

The monochromatic illumination for the IPCE measurements utilized a 300 W xenon arc lamp (Newport) coupled to a 1/8 m grating monochromator (Newport CS130), which was equipped with order sorting filters. The incident power was measured with an optical power meter (Newport 1918 C) and a UV-enhanced Si photodiode sensor. The IPCE is calculated based on the following equation,

$$\text{IPCE} = \frac{1240 \times i}{P_{\text{light}} \times \lambda} \quad (4)$$

where i is the steady-state photocurrent density at a specific wavelength λ of the incident, and P_{light} is the light intensity for the specific wavelength (λ). The impedance of the electrochemical cell (Z) was measured under dark conditions at a series of electrode potentials, in the frequency (f) range 10² to 10⁵ Hz.

Conflicts of interest

There are no conflicts to declare.

Acknowledgements

We acknowledge funding support from the National Science Foundation (#1254600). This research used resources of the Center for Functional Nanomaterials, which is a U. S. DOE Office of Science Facility, at Brookhaven National Laboratory under Contract No. DE-SC0012704.

Notes and references

- G. Hodes, D. Cahen and J. Manassen, *Nature*, 1976, **260**, 312–313.
- M. Carmo, D. L. Fritz, J. Merge and D. Stolten, *Int. J. Hydrogen Energy*, 2013, **38**, 4901–4934.



- 3 V. S. Vidyarthi, M. Hofmann, A. Sayan, K. Sliozberg, D. Konig, R. Beranek, W. Schuhmann and A. Ludwig, *Int. J. Hydrogen Energy*, 2011, **36**, 4724–4731.
- 4 M. Ma, K. Zhang, P. Li, M. S. Jung, M. J. Jeong and J. H. Park, *Angew. Chem., Int. Ed. Engl.*, 2016, **55**, 11819–11823.
- 5 M. Balandeh, A. Mezzetti, A. Tacca, S. Leonardi, G. Marra, G. Divitini, C. Ducati, L. Meda and F. Di Fonzo, *J. Mater. Chem. A*, 2015, **3**, 6110–6117.
- 6 S. Shin, H. S. Han, J. S. Kim, I. J. Park, M. H. Lee, K. S. Hong and I. S. Cho, *J. Mater. Chem. A*, 2015, **3**, 12920–12926.
- 7 H. Wang, T. Lindgren, J. He, A. Hagfeldt and S.-E. Lindquist, *J. Phys. Chem. B*, 2000, **104**, 5686–5696.
- 8 T. Li, J. He, B. Pena and C. P. Berlinguette, *ACS Appl. Mater. Interfaces*, 2016, **8**, 25010–25013.
- 9 Y. Liu, J. Li, W. Li, H. He, Y. Yang, Y. Li and Q. Chen, *Electrochim. Acta*, 2016, **210**, 251–260.
- 10 Y. Liu, J. Li, W. Z. Li, Y. H. Yang, Y. M. Li and Q. Y. Chen, *J. Phys. Chem. C*, 2015, **119**, 14834–14842.
- 11 Y. Liu, J. Li, H. Tang, W. Z. Li, Y. H. Yang, Y. M. Li and Q. Y. Chen, *Electrochem. Commun.*, 2016, **68**, 81–85.
- 12 Y. Liu, Y. Yang, Q. Liu, Y. Li, J. Lin, W. Li and J. Li, *J. Colloid Interface Sci.*, 2018, **512**, 86–95.
- 13 Y. Liu, Y. H. Yang, Q. Liu, H. Z. He, W. H. Liu, D. D. Meng, Y. M. Li, W. Z. Li and J. Li, *Int. J. Hydrogen Energy*, 2018, **43**, 208–218.
- 14 J. Yan, T. Wang, G. Wu, W. Dai, N. Guan, L. Li and J. Gong, *Adv. Mater.*, 2015, **27**, 1580–1586.
- 15 C. A. Bignozzi, S. Caramori, V. Cristino, R. Argazzi, L. Meda and A. Tacca, *Chem. Soc. Rev.*, 2013, **42**, 2228–2246.
- 16 A. Tacca, L. Meda, G. Marra, A. Savoini, S. Caramori, V. Cristino, C. A. Bignozzi, V. Gonzalez Pedro, P. P. Boix, S. Gimenez and J. Bisquert, *ChemPhysChem*, 2012, **13**, 3025–3034.
- 17 R. H. Coridan, K. A. Arpin, B. S. Brunschwig, P. V. Braun and N. S. Lewis, *Nano Lett.*, 2014, **14**, 2310–2317.
- 18 J. M. Spurgeon, J. M. Velazquez and M. T. McDowell, *Phys. Chem. Chem. Phys.*, 2014, **16**, 3623–3631.
- 19 C. C. McCrory, S. Jung, I. M. Ferrer, S. M. Chatman, J. C. Peters and T. F. Jaramillo, *J. Am. Chem. Soc.*, 2015, **137**, 4347–4357.
- 20 J. W. Huang, Y. Zhang and Y. Ding, *ACS Catal.*, 2017, **7**, 1841–1845.
- 21 J. Zhang, Z. Liu and Z. Liu, *ACS Appl. Mater. Interfaces*, 2016, **8**, 9684–9691.
- 22 C. Liu, Y. Yang, W. Li, J. Li, Y. Li and Q. Chen, *Sci. Rep.*, 2016, **6**, 23451.
- 23 C. Cheng, J. Shi, Y. Hu and L. Guo, *Nanotechnology*, 2017, **28**, 164002.
- 24 J. Cen, Q. Wu, M. Liu and A. Orlov, *Green Energy & Environment*, 2017, **2**, 100–111.
- 25 H. Hamdi, E. K. H. Salje, P. Ghosez and E. Bousquet, *Phys. Rev. B*, 2016, **94**, 245124.
- 26 J. M. Berak and M. J. Sienko, *J. Solid State Chem.*, 1970, **2**, 109–133.
- 27 M. Sarnowska, K. Bienkowski, P. J. Barczuk, R. Solarska and J. Augustynski, *Adv. Energy Mater.*, 2016, **6**, 1600526.
- 28 G. M. Wang, Y. C. Ling, H. Y. Wang, X. Y. Yang, C. C. Wang, J. Z. Zhang and Y. Li, *Energy Environ. Sci.*, 2012, **5**, 6180–6187.
- 29 O. Zandi, A. R. Schon, H. Hajibabaei and T. W. Hamann, *Chem. Mater.*, 2016, **28**, 765–771.
- 30 M. F. Daniel, B. Desbat, J. C. Lassegues, B. Gerand and M. Figlarz, *J. Solid State Chem.*, 1987, **67**, 235–247.
- 31 C. Santato, M. Odziemkowski, M. Ulmann and J. Augustynski, *J. Am. Chem. Soc.*, 2001, **123**, 10639–10649.
- 32 C. V. Ramana, S. Utsunomiya, R. C. Ewing, C. M. Julien and U. Becker, *J. Phys. Chem. B*, 2006, **110**, 10430–10435.
- 33 I. M. Szilagyi, B. Forizs, O. Rosseler, A. Szegedi, P. Nemeth, P. Kiraly, G. Tarkanyi, B. Vajna, K. Varga-Josepovits, K. Laszlo, A. L. Toth, P. Baranyai and M. Leskela, *J. Catal.*, 2012, **294**, 119–127.
- 34 S. K. Deb, *Phys. Rev. B*, 1977, **16**, 1020–1024.
- 35 M. Z. Liu, J. L. Lyons, D. H. Yan and M. S. Hybertsen, *Adv. Funct. Mater.*, 2016, **26**, 219–225.
- 36 A. J. Bard and L. R. Faulkner, *Electrochemical Methods: Fundamentals and Applications*, Wiley, NJ, US, 2 edn, 2000.
- 37 J. Cen, Q. Wu, D. Yan, J. Tao, K. Kisslinger, M. Liu and A. Orlov, *Phys. Chem. Chem. Phys.*, 2017, **19**, 2760–2767.
- 38 H. D. Zheng, J. Z. Ou, M. S. Strano, R. B. Kaner, A. Mitchell and K. Kalantar-Zadeh, *Adv. Funct. Mater.*, 2011, **21**, 2175–2196.
- 39 W. Li, P. Da, Y. Zhang, Y. Wang, X. Lin, X. Gong and G. Zheng, *ACS Nano*, 2014, **8**, 11770–11777.
- 40 M. A. Butler, *J. Appl. Phys.*, 1977, **48**, 1914–1920.
- 41 R. A. Pala, A. J. Leenheer, M. Lichterman, H. A. Atwater and N. S. Lewis, *Energy Environ. Sci.*, 2014, **7**, 3424–3430.
- 42 Q. Shi, S. Murcia-Lopez, P. Y. Tang, C. Flox, J. R. Morante, Z. Y. Bian, H. Wang and T. Andreu, *ACS Catal.*, 2018, **8**, 3331–3342.
- 43 F. Le Formal, N. Tétreault, M. Cornuz, T. Moehl, M. Grätzel and K. Sivula, *Chem. Sci.*, 2011, **2**, 737–743.
- 44 G. M. Carroll and D. R. Gamelin, *J. Mater. Chem. A*, 2016, **4**, 2986–2994.
- 45 W. R. Zhang, D. H. Yan, J. Li, Q. Y. Wu, J. J. Cen, L. H. Zhang, A. Orlov, H. L. Xin, J. Tao and M. Z. Liu, *Chem. Mater.*, 2018, **30**, 1677–1685.
- 46 R. Zhang, F. Ning, S. Xu, L. Zhou, M. Shao and M. Wei, *Electrochim. Acta*, 2018, **274**, 217–223.

